Can tectonic processes be recovered from new gravity satellite data?

Valentin Mikhailov[a,b], Sergei Tikhotsky[a], Michel Diament[b,*],
Isabelle Panet[b,c], Valérie Ballu[b]

[a]*Institute of Physics of the Earth, Russian Academy of Sciences, B. Gruzinskaya 10, Moscow, Russia*
[b]*Laboratoire de Gravimétrie et Géodynamique, Département de Géophysique Spatiale et Planétaire (UMR CNRS/IPGP/Paris7 7096),
Institut de Physique du Globe de Paris, Case 89, 4 Place Jussieu, 75252 Paris Cedex 05, France*
[c]*Laboratoire de Recherche en Géodésie, Institut Géographique National, ENSG, 6 et 8 av. Blaise Pascal, Cité Descartes,
77455 Marne-la-Vallée Cedex, France*

Received 26 April 2004; received in revised form 24 September 2004; accepted 27 September 2004
Available online 11 November 2004
Editor: V. Courtillot

Abstract

The goal of this study is to investigate whether temporal variations of the gravity field caused by tectonic processes (hereafter geodynamic signals) can be recognized in satellite gravity data, including the currently operating GRACE satellites and future systems. We restricted our study to subduction zones, calculating possible gravity field variations associated with elastic stress accumulation in locked areas and with stress release by earthquakes. We used fault-plane solutions for the Alaska-1964, Chile-1960 and Hokkaido-2003 earthquakes, and GPS-based strain accumulation data in locked areas of the Alaska subduction zone. Vertical displacements of the Earth's surface were calculated using a model of a rectangular fault in an elastic half-space. We developed and applied a statistical signal-recognition technique to identify signals caused by displacements of unknown magnitude on fault planes of given position and dimension. Our goal is thus to detect and analyse in satellite gravity data a signal constrained by ground geophysical and geodetic data. We assumed different levels of data accuracy, ranging from the first GRACE model GGM-01S to two orders of magnitude lower, corresponding to the target accuracy for GRACE and GOCE data. We concluded that using the developed technique, gravity field variations similar to those caused by Alaska-1964 earthquake should be recognizable in GRACE data at the accuracy level of the model GGM-01S. If forthcoming satellite gravity models have an accuracy one order of magnitude better, then the signal recognition probability will be about 99% using our approach. The required accuracy is close to the errors due to imperfect corrections for atmospheric effects. For the Chile-1960 earthquake we considered different fault-plane models and found that one can distinguish between these models with a probability approaching 70% at present level of GRACE accuracy. Increasing the data accuracy by one order of magnitude makes this probability very high. Because the gravity signal from the Hokkaido-2003 earthquake was rather weak, it would only be recognized if the data accuracy increases by two orders of magnitude thus approaching the target GRACE accuracy. If forthcoming gravity models are one

order of magnitude more accurate compared to the first GRACE model then 5 years of data will allow recognition of time varying gravity signal associated with locked areas of the Alaska subduction zone. Our method may be easily applied to other geodynamic targets and more generally be adapted to other time varying gravity studies.

1. Introduction

In the past few years, our knowledge of the Earth gravity field and its temporal variations was considerably improved thanks to dedicated satellite missions. Presently operating (CHAMP, GRACE) and planned (e.g. GOCE) satellite missions are opening an exciting new era in the remote study of the Earth using gravity data. The GRACE satellite system, launched in 2002, was designed to increase the accuracy of global Earth gravity models by several orders of magnitude and to monitor temporal variations of the gravity field for the first time [1]. The GOCE satellite, to be launched in 2006, will provide even higher accuracy gravity field models (up to 250 spherical harmonics) [2].

GRACE was designed to produce a new global gravity field model every 3–5 weeks during its 5-year lifetime, allowing the identification of temporal variations of the global gravity field and contributing to various branches of Earth sciences, including the study of crustal and upper mantle structure and geodynamic monitoring of tectonically active regions. GOCE should provide several global gravity field models of even higher accuracy, making it possible to study shorter wavelength components in temporal variations of the gravity field. Mission scheduling includes two 6-month measurement periods separated by a 5-month period during which the satellite will be boosted to a higher orbit. During each 6-month period three Earth gravity field models will be constructed by integrating data from two months of measurements [3].

The first global GRACE gravity field model, named GGM-01S, was issued in 2003. It includes spherical harmonics up to degree 120 with half-wavelengths longer than 170 km. This model is almost two orders of magnitude more accurate than the gravity models based on data from all previous satellite missions (e.g. EGM-96). GRACE baseline accuracy is almost two orders of magnitude smaller than GGM-01S accuracy (Fig. 1). GOCE will improve the resolution to wavelengths as short as 100 km with a cumulative error of about 1 cm in the geoid height or 1 mGal in the gravity field. Several follow-on missions are currently under discussion or preparation in the USA and Europe.

The main goals of the GRACE mission are to monitor climate changes and to study atmospheric and global oceanic circulation processes for environmental purposes. GRACE also records short-term variations caused, for instance, by atmospheric processes, snow thickness changes, soil humidity changes or modification of the ice-sheet balance. Geodynamic processes such as changes in the Earth's topography or mass distribution as a result of lithospheric plate interactions (collision, subduction, rifting), postglacial rebound, mantle convection, earthquakes, sedimentation and erosion, should also contribute to temporal variations of the Earth gravity field.

Several studies have been devoted to quantitative estimates of the contribution of regional geodynamic processes to temporal variations of the Earth's gravity field. Velicogna and Wahr [4] addressed the effect of postglacial rebound and the possibility of recovering mantle viscosity profiles using satellite data, and concluded that GRACE data could significantly contribute to solve this problem. In a very recent paper, Sun and Okubo [5] compared the GRACE target accuracy to degree amplitude spectra for coseismic deformations resulting from the 1964 and 2002 Alaska, and 2003 Hokkaido earthquakes. They concluded that coseismic deformations for an earthquake with a seismic magnitude above 7.5 could be detected by GRACE.

Here we do not only compare the relative amplitude of geodynamic signal and instrumental noise, but we
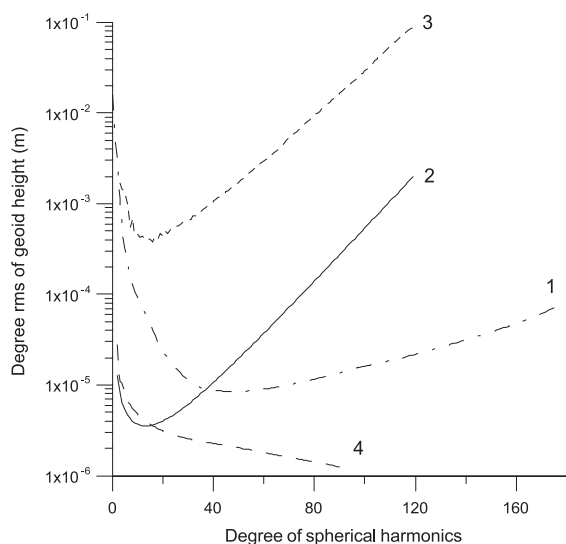
Fig. 1. Accuracy of spherical harmonics in different geoid height models. (1) GOCE (target mission accuracy); (2) GOCE (target mission accuracy); (3) the first GRACE models GGM-01S. Gravity anomaly half-wavelength $\lambda/2$ is related to the degree of spherical harmonic l by the relation: $\lambda/2 \approx 110 \times (180/l)$ km.

also evaluate the probability of correctly interpreting temporal series of space gravity data, i.e. of retrieving a geodynamic signal when it is really present. To do so, we take into account a priori information on the investigated signal using surface geodetic or geophysical data, as well as the variance of the noise. This last incorporates instrumental errors and mismodelling of the other sources of temporal gravity variations. Besides, let us notice that a direct comparison of energy spectra should be carefully interpreted, since the spherical harmonic spectrum "dilutes" the effect of a local signal on the whole sphere, and may lead to over-pessimistic conclusions. More precisely, we consider here global gravity field variations resulting from the dynamics of subduction zones. We investigate whether satellite gravity data can be used to quantify processes of elastic stress accumulation and its release through earthquakes. We address two questions: (1) Can satellite data be used to recover some characteristics of the seismic deformations and thus to estimate parameters of the fault plane? To answer, we first check that seismic signals can be detected in GRACE data, then we investigate if GRACE data can help in constraining the fault plane

parameters; (2) Can satellite gravity data be used to monitor the elastic stress accumulation in locked areas of subduction zones?

For our purpose, we use the first GRACE model GGM-01S, available at http://www.csr.utexas.edu/grace/gravity. For technical reasons, this model is almost two orders of magnitude less accurate than GRACE baseline accuracy. However, it is very likely that the accuracy of the following GRACE models will increase; hopefully it will reach the planned accuracy. Moreover, we do not restrict our consideration to GRACE data, as it has been done in [5], but investigate perspectives of geodynamic signal recognition from global gravity in order to set accuracy requirements for future satellite missions. Our results therefore apply to future as well as current data and satellite missions.

2. Deformation and gravity changes expected in subduction zones

In general, the geodynamics of subduction zones are poorly constrained. Dense geodetic networks and precise repeated levelling usually do not cover the area needed for proper modelling. This is due to the fact that most (if not all) high strain area is usually situated in the oceanic domain and cannot be surveyed by routine geodetic instruments. As a result, even for the greatest earthquakes, such as Chile-1960, geodetic surveys only registered surface displacements in regions far from the epicentral zone, not permitting a unique determination of the fault plane position and parameters [6].

Seismology and geodetic data show that subduction is not a continuous process. In some areas, the rate of subduction is lower than the rate of lithospheric plate convergence. These areas are referred to as partly or completely locked. In these areas, subduction recommences when the accumulated stress becomes larger than the locking stress threshold. The locking stress apparently depends upon a number of factors including the topography of the plate interfaces, the dip of the sinking plate, the thermal state (i.e. age of the plate) and the presence of water and sediments in the coupling zone. The stress can be released as an earthquake or a slow aseismic thrust event.

Huge amounts of data on the dynamics of locked areas of subduction zones have been collected by the Japanese geodetic network GEONET. This network, established in 1994, includes about 1000 stations separated by an average distance of 25 km [7]. It allows to monitor the position and dimension of locked areas and to register slow thrust events leading to aseismic release of accumulated elastic energy. For example, a slow thrust event in the Bungo Channel, separating Shikoku and Kyushu islands (south-western Japan), lasted about 300 days and led to an energy release equivalent to a 6.6 earthquake [8,9]. Below, we will show how high-accuracy satellite gravity data can help to constrain fault plane parameters and to monitor stress accumulation and release in locked areas of subduction zones, including silent slip events which are not recorded by world seismological networks.

Solution for a point or finite source in an elastic half-space based on dislocation theory is the main tool for the mathematical description of stress accumulation and release in locked areas of subduction zones [e.g. [10–13]]. This model describes the earthquake motion releasing the stress accumulated during the locked period of a subduction zone. Savage [14] suggested that the same model could be used to mathematically describe the stress accumulation process. In Savage's [14] model, the velocity field is divided into two components. The first component corresponds to a non-locked subduction with a velocity derived from the plate convergence rate. The second component represents a movement in the opposite direction that is localized at the locked portion of the slab. Depending on the coupling ratio, the sum of two components at the locked portion can be smaller than the plate convergence rate or equal to zero. This model suggests that the first component (subduction) does not produce any stress, whereas the second one (thrusting) causes the stress accumulation that can be described by the dislocation model.

Most studies use an analytical solution for finite sources in an elastic half-space (e.g. [12]), but more sophisticated models have been suggested. Sun and Okubo [15,16] considered the free surface deformation and consequent variations of the gravity field for a single dislocation or for dislocations on a finite fault, in a homogeneous spherical Earth. Ma and Kusznir [17] obtained a solution for layered elastic media and investigated faulting as a result of lithospheric extension. Spherical self-gravitating models of viscoelastic layered media were considered in [18–21].

As a first approach, we use a simple elastic half space model, neglecting the Earth's sphericity. The impact of Earth's sphericity was estimated by Sun and Okubo [15], they concluded that this effect is small in the area of main deformations. More precisely, the discrepancy on ground does not exceed 10 per cent within an epicentral distance of about $10°$. Thus for a low altitude satellite as gravity satellites our first order approximation is reasonable.

Formulas for the components of the displacement vector at the free surface of an elastic half-space with Lamé parameters λ and μ caused by movements on a finite rectangular fault were obtained by integrating a solution for a single dislocation (see e.g. [13]). The used coordinate system and the notation of fault plane parameters are given in Fig. 2. Formulas for the components of the displacement vector are listed in Appendix A.

When the fault surface is approximated by a single plane, components of the displacement vector depend on nine parameters: the size of the fault plane (L,W), the depth to its lower edge (d), the fault orientation (δ, φ), two parameters of the displacement vector $(|\mathbf{U}|=a$ and $\gamma)$, and two coordinates specifying the geographical position of the fault (e.g. the longitude and the latitude of the origin). An a
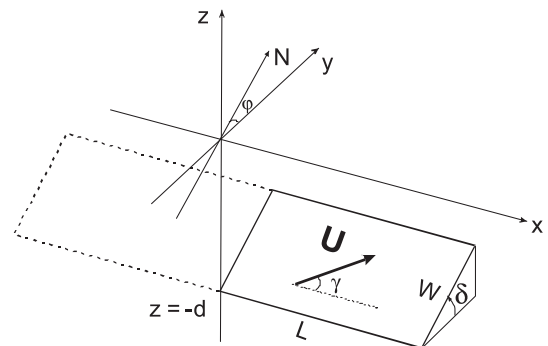

Fig. 2. Definition of fault plane parameters. A fault length is $2L$, W is its dimension downdip, d is the depth to its lower edge, δ is fault's dip, φ is an angle measured from the North to Oy axis clockwise, and γ is an angle measured between direction of displacement vector $\mathbf{U}$ ($|\mathbf{U}|=a$) and direction of Ox axis also clockwise.

priori value can be assigned to some of these parameters. Indeed, one can impose δ and φ to coincide with strike and dip of the subducting plate or when studying an earthquake, one can use a fault plane solution to constrain (δ, φ) and the dimension of the fault plane. Recently Vallée and Bouchon [22] published a method to estimate all fault plane parameters using data from the world seismological networks. Seismological data may also be useful for estimating parameters of locked intervals of a subduction zone. For example, parameters of the planes approximating the rupture zone of the Alaska-1964 earthquake estimated by Christensen and Beck [23] are close to the parameters of the present-day locked asperities estimated by Zweck et al. [24] from detailed geodetic data. For all subduction zones there are estimates of the direction of convergence, which provide an estimate of the angle λ. When the subduction zone is completely locked, a is equal to the convergence rate, otherwise it depends on the coupling ratio, which varies from 0 to 1 in partly locked zones and can be negative in regions of postseismic restoration. Since a can only be estimated from the results of detailed repeated geodetic measurements, it cannot generally be a priori defined.

Thus, the dynamic of subduction zones is not fully constrained by surface measurements. We now investigate how satellite gravity data, combined with ground data, may help in understanding and monitoring subduction zones.

3. A statistical approach for recognizing and discriminating geodynamic signals in subduction zones from gravity field variations

The geoid height $u(\theta, \varphi, t_i)$ measured by satellites can be written as the sum of three components: a stationary component $\bar{u}(\theta, \varphi)$, a temporal variation component of geodynamic origin $u^G(\theta, \varphi, t_i)$, and a noise component $\delta u(\theta, \varphi, t_i)$, i.e.:

$$u(\theta, \varphi, t_i) = \bar{u}(\theta, \varphi) + u^G(\theta, \varphi, t_i) + \delta u(\theta, \varphi, t_i),$$
$$i = 1, ..., M, \qquad (1)$$

where: θ and φ are colatitude and longitude and M is the number of satellite gravity models, each of them

relating to a time t_i. We assume hereafter that the gravity data have already been corrected for mass redistribution in the ocean and atmosphere and for continental water storage. Methodology and error estimates for these corrections have been examined in [25,26]. Thus, the noise $\delta u(\theta, \varphi, t_i)$ includes measurement errors, errors due to imperfect corrections for the redistribution of masses in the Earth's fluid envelops, and probably some other geoid temporal variations of unknown origin.

Consecutive satellite geoid models relating to a point of time t_i will be constructed and distributed as a set of coefficients of spherical expansion:

$$N(\theta, \varphi) = \sum_{l=2}^{L} \sum_{m=0}^{l} (C_{lm}\cos(m\varphi) + S_{lm}\sin(m\varphi)) P_l^m(\cos\theta)$$
$$(2)$$

where P_l^m are fully normalized associated Legendre functions, coefficients C and S are measured in units of length (meters) and L is the highest degree in spherical harmonic decomposition.

Using the spherical expansion (Eq. (2)) one can rearrange Eq. (1) to the following form:

$$\begin{Bmatrix} C_{lm}(t_i) \\ S_{lm}(t_i) \end{Bmatrix} = \begin{Bmatrix} \bar{C}_{lm} \\ \bar{S}_{lm} \end{Bmatrix} + \begin{Bmatrix} \tilde{C}_{lm}(t_i) \\ \tilde{S}_{lm}(t_i) \end{Bmatrix} + \begin{Bmatrix} \delta C_{lm}(t_i) \\ \delta S_{lm}(t_i) \end{Bmatrix},$$
$$l = 2, ..., L; m = 0, ..., l; i = 1, ..., M, \qquad (3)$$

where C_{lm} and S_{lm} are spherical expansion coefficients of the geoid height corrected for the ocean, atmosphere, continental water storage and glacial rebound contributions; $\bar{C}_{lm}$ and $\bar{S}_{lm}$ are coefficients of the spherical expansion of the stationary geoid component $\bar{u}(\theta, \varphi)$, $\tilde{C}_{lm}$ and $\tilde{S}_{lm}$ are coefficients corresponding to geodynamic signal $u^G(\theta, \varphi, t_i)$, and δC_{lm} and δS_{lm} are expansion coefficients of the noise including instrumental errors and mismodelling of the other contributions to the temporal variations of the geoid. To shorten the equations, we will use the following notation for all spherical expansion coefficients:

$$Q_{lmk}^i = \begin{cases} C_{lm}(t_i), & k = 0 \\ S_{lm}(t_i), & k = 1 \end{cases}, \qquad (4)$$

keeping the additional indexes corresponding to different geoid components as in Eq. (3).

Further we will treat the coefficients of spherical expansion of the noise $\delta u(\theta, \varphi, t_i)$ as normally distributed random variables with zero expectation vector and given covariance matrix, which incorporates covariances of measurement errors and covariances of unmodelled temporal variations of non-geodynamic origin (these two error sources can be treated as independent). Covariances of the measurements errors are estimated in the course of the satellite data processing and should be available with the geoid spherical expansion coefficients. In the first GRACE model GGM-01S it is supposed that errors in the harmonics of different order are independent (i.e. the covariance matrix is diagonal). For the satellite CHAMP the full covariance matrix is available. It is likely that the full covariance matrix will be available for the other satellite missions as well. Covariances of the errors introduced by different corrections can be estimated by comparing different global data sets (atmospheric pressure, snow thickness, soil humidity) compiled by different meteorological centres, as was done in [25,26], even if this could lead to underestimated errors due to the non-independence of the compared models. Velicogna et al. [26] showed that the accuracy of the correction for atmospheric effects was approximately one order of magnitude better than the accuracy of the GGM-01S model. The largest errors are in fact due to the poor knowledge of continental hydrology. Corrections for hydrology are difficult to estimate precisely since the existing hydrological models considerably differ. Ramillien et al. [27] showed that the precision of correction for hydrology could be of the same order as GGM-01S model errors. In addition, one has to keep in mind that these are mean estimates although hydrological effects are spatially localized. We assume that the errors associated to these various corrections are gaussian. The cumulative errors will also have a normal distribution as the contributions are considered as independent. Finally, we suppose that coefficients δQ^i_{lmk} having different indexes l, m, k, i are not independent, but that their combined probability distribution is a multidimensional normal distribution with zero mean vector and given covariance matrix.

Gravity signals associated with many geodynamical processes can be presented as a product:

$$u^G(\theta, \varphi, t) = a \cdot f(\theta, \varphi) g(t), \qquad (5)$$

where parameter a measured in unit of length stands for the magnitude of the geodynamic process (displacement at the fault plane or rate of displacement at partly locked asperity of subduction zone multiplied to time period under consideration T, etc.), $f(\theta, \varphi)$ is a dimensionless function specifying the form of the geodynamic gravity signal normalized to the magnitude of a, and $g(t) \in [0, 1]$ is a dimensionless function determining the variation of the signal in time. The time constants of strain accumulation processes at locked intervals of subduction zones is considerably larger than the life-time of satellite systems. Besides, geodetic data, for example, data from the Japanese GEONET system [7], show a nearly time-linear growth of lithospheric shortening across the locked intervals of the subduction zone. In this case the time dependence can be presented as a linear function: $g(t)=(t-t_0)/T$, where t_0 is a reference point in time and the parameter a in Eq. (5) is a product of the convergence rate by the coupling ratio and the time period (T) under consideration. For the strain induced by an earthquake one can assign: $g(t)=\sigma(t-t_0)$, where $\sigma(t)$ is a Heaviside step function and parameter a is the displacement amplitude on the fault plane.

Using Eqs. (4), (5), Eq. (3) can be transformed to:

$$Q^i_{lmk} = \bar{Q}_{lmk} + a \cdot \tilde{Q}_{lmk} \cdot g(t) + \delta Q^i_{lmk}, \qquad (6)$$

where $\tilde{Q}_{lmk}$ are the coefficients of expansion of the normalized form of the geodynamic signal $f(\theta, \varphi)$.

After obtaining M successive geoid models, the stationary part of the geoid height $\bar{u}(\theta, \varphi)$ can be estimated by correcting each geoid model for known factors and averaging all M models. When using this approach, an average value should be also subtracted from function $g(t)$. In terms of spherical expansion coefficients one obtains:

$$\bar{Q}_{lmk} = \frac{1}{M} \sum_{i=1}^{M} Q^i_{lmk}. \qquad (7)$$

Then, the residual time-varying part is:

$$\Delta Q^i_{lmk} = Q^i_{lmk} - \bar{Q}_{lmk}, \tag{8}$$

Assuming that the estimate errors of the same spherical coefficients in different gravity field models are independent, hence that their standard deviations do not depend on time and are equal to σ^2_{lmk}, one finds that the standard deviations of spherical coefficients of temporal variations (Eq. (8)) are equal to $(1+1/M)\sigma^2_{lmk}$.

We now test if the residual (Eq. (8)) is either dominated by noise or by the searched signal. Here two types of errors could occur: to make a wrong conclusion that the data contain a signal when there is no signal (false alarm), or to conclude that the data do not contain a signal when in reality a signal is present (signal missing). Our aim is to estimate the corresponding probabilities of errors for different geodynamic signals and different amplitudes of the noise in the satellite data.

The procedure of decision making reduces to verification of the statistical hypothesis H that the difference (Eq. (8)) is a noise, i.e. that its spherical expansion coefficients are random values having multidimensional normal distribution with zero expectation vector and given covariance matrix $\mathbf{C}$, against the alternative K (probably a composite one) that ΔQ^i_{lmk} also possesses a multidimensional normal distribution with the same covariance matrix $\mathbf{C}$, but that the components of its expectation vector are equal to $\tilde{Q}_{lmk} \cdot a \cdot g(t)$. If the form of the signal $f(\theta, \varphi)$, the dependence on time $g(t)$ and the amplitude a are known, the alternative is simple. In the opposite case, it is composite and depends on a number of unknown parameters including parameters of functions $f(\theta, \varphi)$ and $g(t)$.

We can consider parameter a to be an unknown value characterized by distribution $w(a)$. In practical applications, one can usually only assign a mean value a_0 and some uncertainty intervals σ_a. Thus, it is reasonable to suggest that w_a is close to a normal distribution with a mean a_0 and a standard deviation σ_a. When a_0 is known precisely, $\sigma_a=0$.

To test the hypothesis that the data contain the searched signal, we compute a likelihood ratio between signal and noise as explained in Appendix A, and compare it with a threshold. This likelihood ratio takes into account the distributions of probabilities on signal and noise, i.e. the a priori information on the signal derived from ground-based geodetic and geophysical measurements, and the amplitude of the cumulative noise incorporating all possible sources of errors. To decide which hypothesis H or K seems more realistic, we choose the threshold following the Neyman-Pearson criteria [28]. Probabilities of false alarm (named α error) and signal missing (named β error) are then derived [28]. By definition, the false alarm error (α error) is an erroneous rejection of the hypothesis H when it is true. In our case, it results in erroneous decision that a geodynamic signal of given shape is present in the temporal gravity variations. The signal missing error (β error) is an acceptance of the hypothesis H when it is false. In our case, it results in erroneous decision that the data do not contain the desired geodynamic signal.

The procedure of testing the statistical hypothesis H is detailed in Section B1 of Appendix B. Based on the peculiarities of the geodynamic problem under study, one should assign some tolerance probability of false alarm α, find the corresponding threshold value F from Eq. (B13) and compare it to the calculated statistic φ^2 (Eq. (B7)). If (B7) is true, then the hypothesis H that the temporal variations do not contain a geodynamic signal has to be rejected at the significance level α. The corresponding probability of signal missing β can be computed from Eq. (B14). In Section 4 we investigate the recognition of different geodynamic signals in satellite data of various accuracies by assigning a tolerance probability of wrong signal detection (false alarm) α and computing the probability of signal missing β.

An important problem to be solved using satellite gravity data is to discriminate between several models. For example, let us examine which of two possible fault plane models I or II better corresponds to the satellite gravity data. To do so, we follow the procedure considered above. We assume that both signals corresponding to models I and II are known including their respective amplitudes a and b. The principle of signal discrimination is the same as previously explained. We test a simple hypothesis H, that coefficients of residuals (Eq. (8)) correspond to a signal associated to model I, i.e. are random values having multidimen-

sional normal distribution with the expectation vector corresponding to signal *I* and covariance matrix **C** equal to the covariance matrix of the noise, against the similar simple hypothesis where components of the expectation vector corresponds to signal associated to model *II* (with the same covariance matrix **C**). The likelihood ratio between both signals is computed, taking into account the different geodynamical parameters and the characteristics of the cumulative noise in the data (see Section B2 of Appendix B). Probabilities of errors are derived for the two possible types of errors: false alarm (signal associated to model *I* is recognized whereas in reality data contain signal associated to model *II*) and signal missing (signal associated to model *I* is not seen whereas it is present).

4. Recovering geodynamic signals in subduction zones

We now apply our method to three cases: (1) to check whether temporal variations of the Earth gravity field can help to recognise an earthquake induced signal assuming that all parameters of the fault plane are known except the modulus of the displacement vector a; (2) to check if it is possible to discriminate between several possible earthquake fault plane models using satellite gravity data; (3) to test the hypothesis that temporal variations contain a geodynamic signal caused by a partly locked fragment of a subduction zone, assuming that all parameters of the partly locked plane are known except the modulus of displacement vector a. The signal recognition procedure is as follows. After assigning parameters to a geodynamic model, we compute the vertical displacement of the Earth's surface $u_z(\theta, \varphi)$ and transform it into a surface density $\sigma_{\mathrm{eqv}}(\theta, \varphi) = \Delta\rho(\theta, \varphi) \cdot u_z(\theta, \varphi)$, with a density contrast $\Delta\rho$ equal to 2.67×10^3 kg/m^3 on land and 1.64×10^3 kg/m^3 at the sea bottom. Then, coefficients of the spherical expansion of the surface density are given by:

$$Q^\sigma_{lmk} = \frac{1}{4\pi} \int_0^\pi \int_0^{2\pi} \sigma_{\mathrm{eqv}}(\theta, \varphi)[(1-k)\cos(m\varphi)$$
$$+ k\sin(m\varphi)]P_l^m(\cos\theta)\sin\theta \mathrm{d}\theta \mathrm{d}\varphi \qquad (10)$$

and transformed into variations of the geoid height using the following formula:

$$\tilde{Q}_{lmk} = \frac{Q^\sigma_{lmk}}{4\pi\bar{\rho}_\oplus(2l+1)}, \qquad (11)$$

where $\bar{\rho}_\oplus = 5.517 \times 10^3$ kg/m^3 is the average Earth density. Gravity effect of the deformation of the underlying Earth due to the surface load is neglected: we will consider only the gravity effect from the Earth's surface deformation, as this surface is the main density interface. This assumption is supported by field measurements at the site of Alaska-1964 earthquake: by comparing the amplitude of the vertical displacements during the earthquake with measured gravity changes, Barnes [29] concluded that the Earth's surface vertical movements explain almost all observed variations of the gravity field.

We investigate the possibility of signal detection or discrimination for different levels of noise. We use expected degree amplitudes of the baseline errors: for GRACE, they were provided by Brooks Thomas and Mike Watkins at Jet Propulsion Laboratory (personal communication) for GOCE, see [2]. We also considered the errors of the first GRACE model GGM-01S (available at http://www.csr.utexas.edu/grace/gravity). We took into account the first 90 harmonics for GRACE, and the first 180 harmonics for GOCE. The first GRACE gravity model was constructed using almost 1 year of data. To estimate degree amplitude of the errors in bimonthly models we multiplied the GGM-01S error estimates by $\sqrt{6}$. We assume that errors due to mismodelling of the other contributions to temporal variations are included in those levels of noise. This hypothesis is realistic for a noise level equal to GGM-01S errors. The lower noise levels can be considered as target amplitudes for the mismodelling errors.

4.1. Detection of signals caused by earthquakes

Now we consider two earthquakes: the magnitude M_{w}=9.2 Alaska earthquake of March 28, 1964 and the magnitude M_{w}=8.1 Hokkaido earthquake of September 26, 2003, which occurred after the launch of the GRACE mission. We thus compare two gravity models: before and after the earthquake.

For the Alaska-1964 earthquake, we used the simple rupture zone model suggested by Savage and Hastie [12]. The model consists of a single plane with parameters: $2L$=600 km, W=200 km, d=51 km, dip angle δ=9°, φ=60°, a=10 m, and γ=90° (for notation of parameters see Fig. 2). The vertical and horizontal components of the displacement vector are shown in Fig. 3 by contours and vectors, respectively. The vertical displacement amplitude varies from −2.2 to 3.9 m.

Table 1 gives the probability of β error (signal missing) as a function of the probability of α error (false alarm), for different satellite gravity data accuracies. These results show that a strong earthquake, such as Alaska-1964, can be detected using the GRACE data even if the data accuracy

is at the level of the first model GGM-01S. The probability of a false alarm and the probability of signal missing for an earthquake similar to the Alaska-1964 one using GGM-01S data are both close to 30% (Table 1). When the data accuracy is one order of magnitude higher, these probabilities approach zero. For the Hokkaido-2003 earthquake we used parameters given by Vallée and Vergoz (http://www.emsc-csem.org/Html/ JAPAN_ValleeVergoz.html). They used an approach based on the analysis of global seismological data [22]. The fault plane parameters are $2L$=80 km, W=130 km, d=62.5 km, δ=28°, φ=259° γ=129°, a=2–3 m. The amplitude of the vertical displacements varies from −0.1 to 0.5 m, corresponding to a geoid height anomaly of 0.11 m.
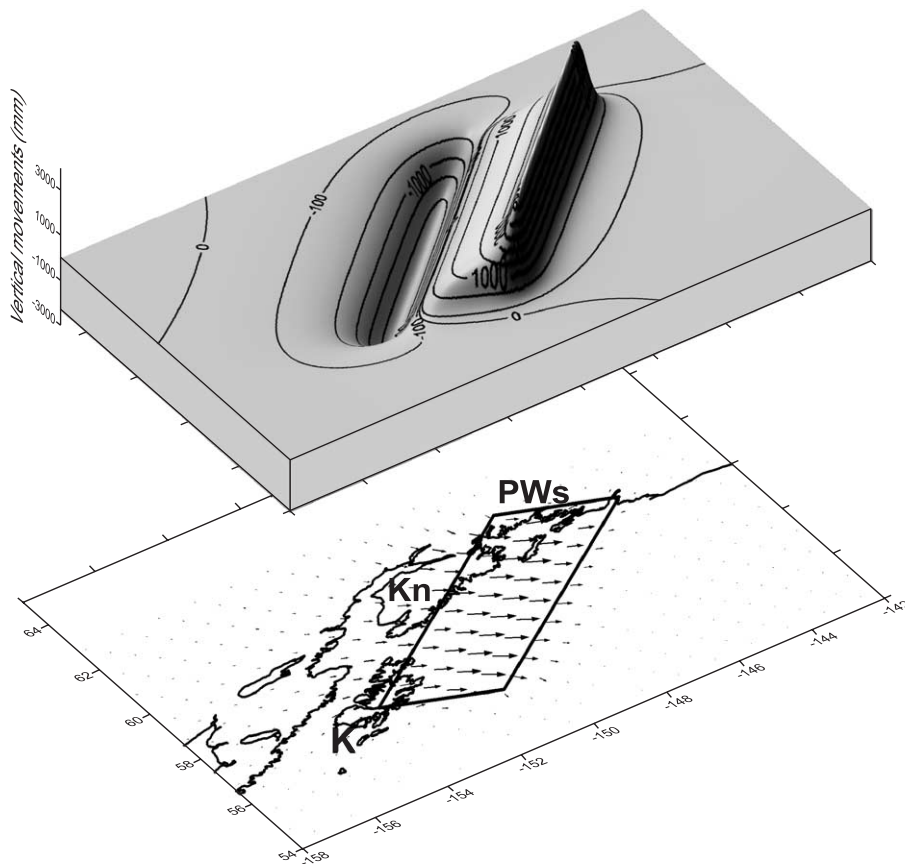

Fig. 3. Vertical displacement of the Earth surface in result of the Alaska-1964 earthquake (meters). Rectangular shows surface projection of the fault plane, corresponding to model 3 of [12]. Arrows show horizontal displacement. Maximal arrow corresponds to 6 m displacement. K—Kodiak island; Kn—Kenai peninsula, PW—Prince William Sound.

Table 1
Probability of signal missing error (β error) depending on given tolerance probability of false alarm (α error for different accuracy of satellite gravity data while detecting the signal from an earthquake)

Probability of false alarm	Probability of signal missing			
	Alaska, 1964, M_w=9.2	Hokkaido-2003, M_w=8.1		
	Accuracy of GGM-01S model	Accuracy of GGM-01S model	Planned GRACE mission accuracy	Planned GOCE mission accuracy
0.1	0.67	0.90	0.56	0.78
0.2	0.51	0.79	0.38	0.63
0.3	0.38	0.69	0.27	0.50

See Section 3 of the text for details. For example, for an earthquake similar to the Alaska-1964 one, using GGM01S data the probability of a false alarm as well as signal missing are close to 0.3. When data accuracy is one order of magnitude higher these probabilities approach to zero (not shown).

The accuracy of the first GRACE model is not sufficient to identify the Earth's surface displacement caused by the Hokkaido-2003 earthquake (Table 1). To characterize this type of earthquake, the accuracy of forthcoming satellite data must achieve the GRACE target level. In this case, the probabilities of a false alarm and of signal missing approach 30%. The probability of a correct signal detection for the planned GRACE mission accuracy appears to be better than the same probability for the planned GOCE mission accuracy, because the main energy of the signal caused by the Hokkaido-2003 earthquake is in the low harmonics ($l<40$), where GRACE data are more accurate than GOCE data (see Fig. 1).

Sun and Okubo [5] used a solution for a point dislocation located in a compressible and self-gravitating spherical Earth to model the gravity signal form the Alaska (1964, 2002) and Hokkaido (2003) earthquakes. We compared the degree amplitude spectrum for a point dislocation used in their study to the spectrum corresponding to the finite rectangular plane of Savage and Hastie [12] and found that these spectra considerably differ. The degree amplitude spectrum for a dip-slip at the large Alaska fault plane decreases rather fast with degree of spherical harmonic. The spectrum for the shallow point dislocation is almost constant or even

increases, thus overestimating possibility to recognize coseismic deformations from satellite data. Anyway, the degree amplitude spectrum corresponding to the Alaska-1964 earthquake is situated below the target GRACE accuracy for harmonics of degree of $n>10$ not depending on the model of the seismic source (we suggest that when comparing spectrum of the Alaska-1964 earthquake to the target GRACE accuracy, Sun and Okubo [5] plotted the solution for the vertical opening instead of the dip-slip on their Fig. 5, thus arriving to the conclusion that Alaska-1964 signal could be seen in the gravity temporal variations).

We should emphasize that we neglected the uncertainties on fault plane parameters in the above examples. However, it would be possible to take them into account (see Section 3 and Appendix A).

4.2. Discrimination between several possible fault plane models using satellite gravity data

Plafker and Savage [6] suggested three possible fault plane models for the Chile-1960 earthquake. The parameters of these models differ (see Fig. 4) because they are poorly constrained by geophysical data. For instance, the surface displacement for all three models is very similar in the geodetic surveyed area (on land, east of longitude 286°, see Fig. 4). The upper boundary of the fault plane is at the sea bottom in models A and B, and at a depth of 20.2 km for model C. For all three models, $2L$ is equal to 1000 km, and φ=97°. Because Plafker and Savage [6] solved a 2D problem, they only determined the component of displacement normal to the fault plane, i.e. λ=90°. The other parameters are for model A: W=75 km, d=52.6 km, δ=44.5°, U=35.4 m. For model B: W=60 km, d=34.8 km, δ=35.5°, U=19.5 m. For model C: W=105 km, d=100 km, δ=49.5°, U=13.7 m. These models lead to very different vertical displacements. The maximal amplitude reaches 19.8 m for model A, 9.9 m for model B and 6.7 m for model C. Fig. 4 shows the vertical displacements and fault plane geometries for the three models along a profile running across the subduction zone.

As previously, we assume that we possess two satellite gravity models: one before and one after the earthquake. Table 2 gives the possibilities of
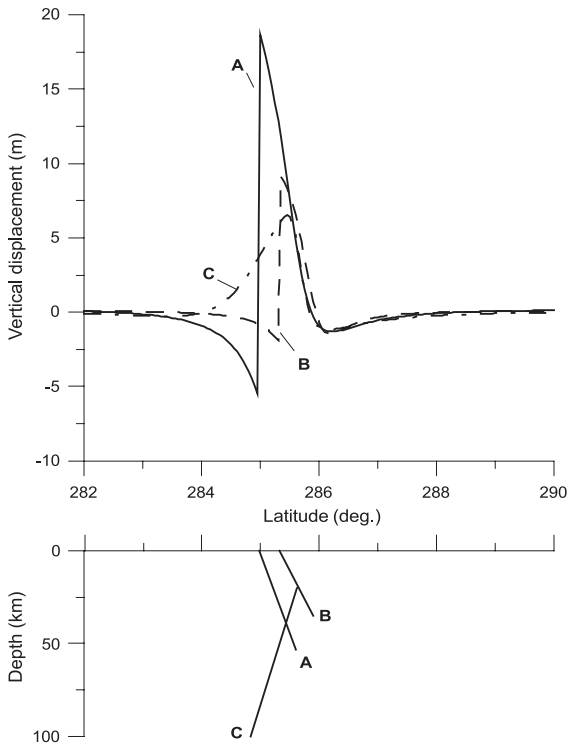
Fig. 4. Three different fault plane models for the Chile-1960 earthquake [9] along the profile running across strike of the Chile subduction zone. Upper graph shows the amplitude of vertical displacements in mm; the lower graph shows position of the fault planes.

from model *B* (these models are most different), with *α*- and *β*-error probabilities close to 0.3. If the satellite data accuracy is one order of magnitude better, the *α* and *β* errors of discriminating between models *A* and *B* or models *A* and *C* approach zero. The error of distinguishing between models *B* and *C* is also small. More accurate satellite gravity data e.g. corresponding to the planned accuracy level for GRACE and GOCE missions will allow to discriminate between fault plane models for smaller magnitude earthquakes.

4.3. Monitoring of the strain accumulation at locked areas of subduction zones

To investigate this problem we used data on the locked asperities of the Alaska subduction zone in the area of the Alaska-1964 earthquake. Several models of locked asperities have been proposed for this region [e.g. [24,30]]. Zweck et al. [24] proposed a detailed model subdividing the area into 1350 fragments of 20×20 km. They characterized every fragment by a specific coupling ratio. All coupling ratios were determined by fitting the calculated Earth's surface displacement to the observed geodetic data. As a result, two completely locked areas were found: one near southwest Prince William Sound and another near southwest Kodiak Island, separated by an area of a small coupling ratio. At the same time, under the western part of Kenai Peninsula and further to the north there is a deep area of reverse slip. The displacement direction in

distinguishing one model from another. Even if the accuracy is identical to the one of the first GRACE model GGM-01S, model *A* can be discriminated

Table 2
Distinguishing between three possible models of the Chile-1960 earthquake fault plane

Probability of the α-error	Probability of the β-error					
	For the accuracy of GGM-01S model			For the accuracy one order of magnitude better the that of GGM-01S model		
	A–B	A–C	B–C	A–B	A–C	B–C
0.01	–	–	–	1.3×10^{-13}	6×10^{-6}	0.13
0.1	0.62	0.73	0.83	–	–	0.016
0.2	0.45	0.57	0.69	–	–	–
0.3	0.33	0.44	0.57	–	–	–

In this specific case, α-error consists in erroneous rejection of the true model A considering alternatives: model A against B or C or erroneous rejection of model B in the alternative: B against C. Consequently, β-error consists in erroneous rejection of an alternative model when it is true. See Section 3 of the text for details. For example, when distinguishing model A from model B and when data accuracy is similar to GGM01S model the probabilities of both α and β errors are 0.3. When data accuracy is one order of magnitude higher these probabilities approach to zero.

this area is opposite to the plate convergence direction and the rate of convergence is 20–30% larger than the mean rate. Zweck et al. [2] explained these movements by post-seismic creep following the Alaska-1964 earthquake.

To investigate the stability of the results, Zweck et al. [2] simplified their model, joining neighbour segments having close coupling ratio values in a single asperity. As a result they found a model containing eight different fault planes. This model provided a good fit to the geodetic data and its main features appeared to be identical to that of the detailed model. We thus computed the strain at the Earth surface in the Alaskan subduction zone using this simplified model. Vertical surface displacements vary between −20 to +25 mm/year in the considered zone. Our computation is validated by field measurements based on GPS and tide gauges [31]. The area where the vertical displacement rate is larger than 10 mm/year measures about 200×700 km^2.

As we discussed above, strain accumulation in locked asperities of subduction zones can be considered as a time-linear function over time intervals of several years (the life period of satellite missions). We estimated the probability of detecting

a linear trend for different possible accuracy levels (see Table 3) assuming that after the 5 year GRACE mission 30 bimonthly satellite gravity models would be available. Table 3 shows that the accuracy of the first model GGM-01S is not sufficient for the linear trend detection. If the accuracy increases by one order of magnitude, the probability of detecting the linear trend is rather high (the probabilities of a false alarm and of signal missing are about 25%). The GOCE satellite has less ability to solve this problem because of the shorter life time of the satellite and small expected number of gravity models (we assumed five models during the two-year mission duration). Thus it appears that it might be possible to monitor vertical movements occurring on the Earth surface at a large scale (typically 200×200 km^2) such as mountainous areas or large sedimentary basins.

5. Summary

In this paper, we applied a statistical signal recognition technique to study the dynamics of subduction zones using time varying satellite gravity data. To do so, we systematically introduce a priori information on the searched signal using ground data. We believe that our method may be easily adapted to other time varying gravity studies (for hydrology, etc.) or to other geodynamic targets (monitoring earthquake cycle, mountain ranges, sedimentary basins, etc.). Our results demonstrate that new satellite gravity data can be used to detect and discriminate geodynamic signals generated by subduction zone dynamics. In particular, to monitor locked asperities of subduction zones or to discriminate between different fault plane models, it is enough to have satellite gravity data whose accuracy is one order of magnitude better than the first GRACE model GGM-01S. It is worth noting that the required accuracy is of the same order of the errors introduced by corrections for atmospheric and hydrology effects. This clearly demonstrates the broad perspectives of studying tectonic processes with the use of forthcoming satellite gravity data. Thus it appears that gravity satellites may be considered in the future as a component of a global monitoring system of the Earth.

Table 3

The probabilities of signal missing with respect to the chosen probabilities of a false alarm when detecting linear-in-time trend in gravity temporal variations dealt with locked fragment of the Alaska subduction zone

Probability of false alarm	Probability of signal missing		
	For the accuracy of GGM-01S model	For the accuracy one order of magnitude better than that of GGM-01S model	Planned GRACE mission accuracy
0.1	0.87	0.47	9×10^{-6}
0.2	0.76	0.30	1.5×10^{-6}
0.3	0.65	0.20	4×10^{-7}

Different possible satellite data accuracy levels are considered. See Section 3 of the text for details. For example, when detecting geodynamic signal from locked area of Alaska subduction zone using satellite data one order of magnitude more accurate than GGM01S model the probability of a false alarm or signal missing is about 0.25.

Appendix A. Formulas for components of displacement vector at the free surface in result of movement at a rectangle fault plane

Components of displacement at the free surface in result of movement on a single fault plane having parameters shown on Fig. 2 are [13]:

$$
\begin{cases}
u_x = -\dfrac{a}{2\pi}\left\{\cos\gamma\left[\dfrac{\xi q}{R(R+\eta)}+\tan^{-1}\dfrac{\xi\eta}{qR}+I_1\sin\delta\right]+\sin\gamma\left[\dfrac{q}{R}-I_3\sin\delta\cos\delta\right]\right\} \\[2mm]
u_y = -\dfrac{a}{2\pi}\left\{\dfrac{\cos\gamma}{R+\eta}\left[\dfrac{\tilde{y}q}{R}+q\cos\delta+I_2\sin\delta(R+\eta)\right]||+\dfrac{\sin\gamma}{R}\left[\dfrac{\tilde{y}q}{(R+\xi)}+\cos\delta\tan^{-1}\dfrac{\xi\eta}{q}-I_1R\sin\delta\cos\delta\right]\right\} \\[2mm]
u_z = -\dfrac{a}{2\pi}\left\{\dfrac{\cos\gamma}{R+\eta}\left[\dfrac{\tilde{d}q}{R}+q\sin\delta+I_4(R+\eta)\sin\delta\right]+\dfrac{\sin\gamma}{R}\left[\dfrac{\tilde{d}q}{(R+\xi)}+\sin\delta\tan^{-1}\dfrac{\xi\eta}{q}-I_5R\sin\delta\cos\delta\right]\right\}
\end{cases}
\tag{A1}
$$

Here, when $\cos\delta\neq0$:

$$I_1 = \frac{\mu}{\lambda+\mu}\left[\frac{-1}{\cos\delta}\frac{\xi}{R+\tilde{d}}\right]-\frac{\sin\delta}{\cos\delta}I_5,$$

$$I_2 = \frac{\mu}{\lambda+\mu}\left[-\ln(R+\eta)\right]-I_3,$$

$$I_3 = \frac{\mu}{\lambda+\mu}\left[\frac{1}{\cos\delta}\frac{\tilde{y}}{R+\tilde{d}}-\ln(R+\eta)\right]+\frac{\sin\delta}{\cos\delta}I_4,$$

$$I_4 = \frac{\mu}{\lambda+\mu}\frac{1}{\cos\delta}\left[\ln\left(R+\tilde{d}\right)-\sin\delta\ln(R+\eta)\right],$$

$$I_5 = \frac{\mu}{\lambda+\mu}\frac{2}{\cos\delta}\tan^{-1}\frac{\eta(X+q\cos\delta)+X(R+X)\sin\delta}{\xi(R+X)\cos\delta},$$

and when $\cos\delta=0$:

$$I_1 = -\frac{\mu}{2(\lambda+\mu)}\frac{\xi q}{\left(R+\tilde{d}\right)^2},$$

$$I_3 = \frac{\mu}{2(\lambda+\mu)}\left[\frac{\eta}{R+\tilde{d}}+\frac{\tilde{y}\,q}{\left(R+\tilde{d}\right)^2}-\ln(R+\eta)\right],$$

$$I_4 = -\frac{\mu}{\lambda+\mu}\frac{q}{R+\tilde{d}},\quad I_5 = -\frac{\mu}{\lambda+\mu}\frac{\xi\sin\delta}{R+\tilde{d}}$$

(when $\cos\delta=0$ there are two cases $\sin\delta=+1$ and -1).

Above we used the following notations: a—modulus of displacement vector U, $p=y\cos\delta+d\sin\delta$, $q=y\sin\delta-d\cos\delta$, $\tilde{y}=\eta\cos\delta+q\sin\delta$, $\tilde{d}=\eta\sin\delta-q\cos\delta$, $R^2=\xi^2+\eta^2+q^2$, $X^2=\xi^2+q^2$. Variables ξ and η were introduced to represent the following substitution: $f(\xi,\eta)=f(x,p)-f(x,p-W)-f(x-L,p)+f(x-L,p-W)$.

Appendix B. Statistical procedure of geodynamic signals recognition and discrimination

B.1. Recognition of geodynamic signal of a given shape

Below we use notations introduced in Section 3. To reduce formulas below, let us introduce the vector of spherical expansion coefficients of gravity temporal variations $\mathbf{x}$ and the vector of spherical coefficients of normalized geodynamic signal $\mathbf{f}$:

$$\begin{aligned} \mathbf{x} &= \{x_n\} = \left\{\Delta Q^i_{lmk}\right\}; \\ \mathbf{f} &= \{f\}n = \left\{\tilde{Q}_{lmk}g(t_i)\right\}. \end{aligned} \tag{B1}$$

The way of numbering the elements (i.e. relation between n and i, l, m, k) is optional. The total number of coefficients is equal to $[(L+1)^2-3]M$, where L is the highest degree in spherical harmonic decomposition, M is number of satellite gravity models (considering temporal gravity variations, we excluded from vectors $\mathbf{x}$ and $\mathbf{f}$ all coefficients with $l<2$ [see [25]] and also do not consider coefficients S_{10} because sin $(mx)\equiv 0$ for $m=0$). Using this notation, the likelihood function of registered gravity temporal variations takes the following form:

$$\begin{aligned} W(\mathbf{x}) &= (2\pi)^{-N/2}(\det\mathbf{C})^{-1/2} \\ &\quad \exp\left\{-\frac{1}{2}(\mathbf{x}-a\mathbf{f})^T\mathbf{C}^{-1}(\mathbf{x}-a\mathbf{f})\right\}, \end{aligned} \tag{B2}$$

where a is amplitude of geodynamic process (see Eq. (6)), supposed to be unknown.

The likelihood ratio is given by the formula:

$$\begin{aligned} \Lambda(\mathbf{x}) &= \int w(a)\exp\left[-\frac{1}{2}(\mathbf{x}-a\mathbf{f})^T\mathbf{C}^{-1}(\mathbf{x}-a\mathbf{f})\right] \\ &\quad \mathrm{d}a/\exp\left\{-\frac{1}{2}\mathbf{x}^T\mathbf{C}^{-1}\mathbf{x}\right\}, \end{aligned} \tag{B3}$$

where $w(a)$ is the probability density of the amplitude of geodynamic signal, and integration performs over all allowable values of a. Eq. (B3) can be transformed to the following form:

$$\Lambda(\mathbf{x}) = \int w(a)\exp\left[ar - \frac{1}{2}a^2d^2\right]\mathrm{d}a \tag{B4}$$

where:

$$r = \mathbf{x}^T\mathbf{C}^{-1}\mathbf{f}$$

$$d^2 = \mathbf{f}^T\mathbf{C}^{-1}\mathbf{f}. \tag{B5}$$

Usually, one can assign only the mean value a_0 and also estimate some uncertainty interval σ_a. Thus, let us suggest that $w(a)$ is close to the normal distribution with the mean a_0 and the deviation σ_a. Substituting probability density function for a normal distribution into (B3) and integrating with respect to a over all real axis, one obtains:

$$\Lambda(\mathbf{x}) = \left(d^2\sigma_a^2 + 1\right)^{-1/2}\exp\left\{-\frac{1}{2}\left(\frac{d^2a_0^2 - r^2 - 2a_0r}{d^2\sigma_a^2 + 1}\right)\right\}. \tag{B6}$$

By taking the logarithm of Eq. (B6), after simple manipulations, one concludes that testing of the hypothesis H reduces to calculation of statistic $\varphi^2=(r+a_0)^2$ and its comparison to a threshold, which depends on chosen optimal criteria. In other words, hypothesis H has to be rejected when:

$$\begin{aligned} \varphi^2 &= (r + a_0)^2 \geq \ln\left[c^2\left(d^2\sigma_a^2 + 1\right)\right]\left(d^2\sigma_a^2 + 1\right) \\ &\quad + a_0^2(d^2 + 1) = F, \end{aligned} \tag{B7}$$

where c is a constant, which depends on chosen optimal criteria. Choosing the appropriate criteria and the corresponding constant c depends on the a priori information available: a priori probabilities of the signal presence, penalties for wrong decisions. If no such information is available then the constant c and, thus, the threshold F could be assigned on the basis of the maximum likelihood or Neyman-Pearson criteria.

We follow the Neyman-Pearson approach in which the threshold F is determined by assigning the tolerance probability of errors of the first and the second kind (see Section 3). For every pair of parameters (a_0, σ_0) of the probability density function, application of the Neyman-Pearson criteria ensures the minimal probability of the second kind error, when probability of the first kind error is assigned. According to the Neyman-Pearson lemma [28] the threshold

F corresponding to the most powerful criterion is determined from the condition:

$$\int_F^\infty W_{\varphi^2}(x|H)\mathrm{d}x = \alpha, \tag{B8}$$

where α is given tolerance probability of the first-kind error, $w_{\varphi^2}(x|H)$ is the probability density function of statistic φ^2 under condition that the hypothesis H is true. Probability of the second kind error in this case is equal to:

$$\beta = \int_{-\infty}^F w_{\varphi^2}\left(x|K, a_0, \sigma_a^2\right)\mathrm{d}x, \tag{B9}$$

where $w_\varphi(x|K, a_0, \sigma_a^2)$ is the probability density function of statistic φ^2, with parameters a_0 and σ_a, and under condition that the alternative hypothesis K is true.

It follows from Eq. (B4) that statistic φ is normally distributed. When the hypothesis H is true, its expectation and variance are:

$$\mathbf{M}_1[r + a_0|H] = a_0, \mathbf{D}[r + a_0|H] = \mathbf{f}^T\mathbf{C}^{-1}\mathbf{f} = s_H^2. \tag{B10}$$

It is easy to show that when alternative K is true, then:

$$\mathbf{M}_1[r + a_0|K] = a_0\left(\mathbf{f}^T\mathbf{C}^{-1}\mathbf{f} + 1\right) = a_K,$$

$$\mathbf{D}[r + a_0|K] = \mathbf{f}^T\mathbf{C}^{-1}\mathbf{f} + \sigma_a^2|\mathbf{C}^{-1}\mathbf{f}|^2 = s_K^2. \tag{B11}$$

The square of a normally distributed variable with the mean b and variance s^2 has the following integral density distribution:

$$F_{\varphi^2}(x) = \int_0^x w_{\varphi^2}(y)\mathrm{d}y = \Phi\left(\frac{\sqrt{x} - b}{s}\right)$$
$$+ \Phi\left(\frac{\sqrt{x} + b}{s}\right) - 1, \quad x > 0, \tag{B12}$$

where $\Phi(x)$ is Laplace's integral.

It follows from Eqs. (B8), (B9) and (B12) that for a given tolerance of false alarm α, the threshold F determines by the formula:

$$\alpha = 2 - \Phi\left(\frac{\sqrt{F} - a_0}{s_H}\right) - \Phi\left(\frac{\sqrt{F} + a_0}{s_H}\right), \tag{B13}$$

and corresponding probability of signal missing is:

$$\beta = \Phi\left(\frac{\sqrt{F} - a_K}{s_K}\right) + \Phi\left(\frac{\sqrt{F} + a_K}{s_K}\right) - 1. \tag{B14}$$

Formulas (B13), (B14) are useful not only for practical applications for signals detection but also for studying of perspectives to hit geodynamic signals in the data of the present and future satellite missions.

B.2. Discrimination of two possible geodynamic models

The procedure to estimate which of two known geodynamic signals is present in temporal variations of the gravity field is as follows. Suppose that there are two theoretical alternative geodynamic signals $f_A^G(\theta, \varphi)$ and $f_B^G(\theta, \varphi)$ corresponding to two different alternative geodynamic models. Let coefficients of their spherical expansion be A_{lmk}^i and B_{lmk}^i. In this case the problem reduces to testing a simple hypothesis H_0, that spherical coefficients of gravity temporal variations $\Delta Q_{lmk}^i = A_{lmk}^i + \delta Q_{lmk}^i$ are random values, having multidimensional normal distribution, covariance matrix $\mathbf{C}$, and expectation vector $f^A = \{f_n^A\}$, where $f_n^A = A_{lmk}^i$. The alternative hypothesis H_1 is that ΔQ_{lmk}^i has the same distribution with the same covariance matrix and expectation vector $\mathbf{f}^B$, which components are f_n^B. The way to number coefficients of matrixes in a vector is optional.

Following the standard recipes of testing statistical hypotheses (e.g. [28]), one obtains that hypothesis H_0 has to be rejected if:

$$\eta = (\mathbf{f}^A - \mathbf{f}^B)^T\mathbf{C}^{-1}\mathbf{x} \leq \ln c - \frac{1}{2}\sum_{i=1}^N \frac{\left(f_i^A\right)^2 - \left(f_i^B\right)^2}{\sigma_i^2} = F \tag{B15}$$

and accepted in the opposite case. Statistic η is distributed normally, so α and β errors are:

$$\alpha = 1 - \Phi\left(\frac{F - \mathbf{M}_1[\eta|H_0]}{\sqrt{\mathbf{D}[\eta|H_0]}}\right),$$

$$\beta = \Phi\left(\frac{F - \mathbf{M}_1[\eta|H_1]}{\sqrt{\mathbf{D}[\eta|H_1]}}\right), \tag{B16}$$

where $\Phi(x)$ is Laplace's integral. Expectation and variance when hypothesis H_0 is true are:

$$\mathbf{M}_1[\eta|H_0] = \left(\mathbf{f}^A - \mathbf{f}^B\right)^T \mathbf{C}^{-1} \mathbf{f}^B;$$
$$\mathbf{D}[\eta|H_0] = \left(\mathbf{f}^A - \mathbf{f}^B\right)^T \mathbf{C}^{-1} \left(\mathbf{f}^A - \mathbf{f}^B\right)$$
(B17)

and when alternative hypothesis H_1 is true are:

$$\mathbf{M}_1[\eta|H_0] = \left(\mathbf{f}^A - \mathbf{f}^B\right)^T \mathbf{C}^{-1} \mathbf{f}^A;$$
$$\mathbf{D}[\eta|H_0] = \left(\mathbf{f}^A - \mathbf{f}^B\right)^T \mathbf{C}^{-1} \left(\mathbf{f}^A - \mathbf{f}^B\right).$$
(B18)

Hence, the procedure of discrimination of two signals is similar to the procedure of signal detection. One assigns the tolerance probability α to reject erroneously the hypothesis H_0, estimates the threshold F from the left equation in (Eq. (B16)); calculates statistic η and verifies inequality (Eq. (B15)). The probability β to make a wrong decision that gravity temporal variations contain the signal $f_A^G(\theta, \varphi)$ when in reality they contain the signal $f_B^G(\theta, \varphi)$ determines by the right equation in Eq. (B16).

References

[1] J.O. Dickey, et al., Satellite Gravity and the Geosphere, National Research Council Report, National Academic Press, Washington, DC, 1997, 112 pp.

[2] M.R. Drinkwater, R. Floberghagen, R. Haagmans, D. Muzi, A. Popescu, GOCE: ESA's first earth explorer core mission, in: G.B. Beutler, M.R. Drinkwater, Rummel R. Von Steiger (Eds.), Earth Gravity Field from Space—from Sensors to Earth Sciences, Space Science Series of ISSI, vol. 18, Kluwer Academic Publishers, Dordrecht, Netherlands, 2003, pp. 419–432.

[3] G. Balmino, R. Rummel, P. Visser, P. Woodworth, Gravity field and steady-state ocean circulation mission. Reports for assessment: the four candidate earth explorer core missions, Eur. Space Agency Rep. SP 1233 (1) (1999) (217 pp.).

[4] I. Velicogna, J. Wahr, Postglacial rebound and Earths viscosity structure from GRACE, J. Geophys. Res. 107 (2002) 2376.

[5] W. Sun, S. Okubo, Coseismic deformations detectable by satellite gravity missions: a case study of Alaska (1964, 2002) and Hokkaido (2003) earthquakes in the spectral domain, J. Geophys. Res. 109 (2004) B04405.

[6] G. Plafker, J.C. Savage, Mechanism of the Chilean earthquakes of May 21 and 22, Geol. Soc. Am. Bull. 81 (1960) 1001–1030 (1970).

[7] S. Zhao, X. Wu, T. Hori, A. Smith, Y. Kaneda, S. Takemoto, Deformation and stress localization at the Nankai subduction zone, southwest Japan, Earth Planet. Sci. Lett. 206 (2003) 145–160.

[8] H. Hirose, K. Hirahara, F. Kimata, N. Fujii, Sh. Miyazaki, A slow thrust slip event following the two 1996 Hyunganada earthquakes beneath the Bungo Chanel, southwest Japan, Geophys. Res. Lett. 26 (1999) 3237–3240.

[9] Sh. Miyazaki, K. Heki, Crustal velocity field of southwest Japan: subduction and arc–arc collision, J. Geophys. Res. 106 (2001) 4305–4326.

[10] J.A. Steketee, On the Volterra's dislocation in semi-infinite elastic medium, Can. J. Phys. 36 (1958) 192–205.

[11] T. Maruyama, Statical elastic dislocations in an infinite and semi-infinite medium, Tokio Univ., Bull. Earthq. Res. Inst. Univ. Tokio 42 (1964) 289–368.

[12] J.C. Savage, L.M. Hastie, Surface deformation associated with dip-slip faulting, J. Geophys. Res. 71 (1966) 4897–4904.

[13] Y. Okada, Surface deformation due to shear and tensile faults in a half-space, Bull. Seismol. Soc. Am. 75 (1985) 1135–1154.

[14] J.C. Savage, A dislocation model of strain accumulation ad release at a subduction zone, J. Res. 88 (1983) 4984–4996.

[15] W. Sun, S. Okubo, Surface potential and gravity changes due to internal dislocations in spherical Earth. I: theory for a point dislocation, Geophys. J. Int. 114 (1993) 569–592.

[16] W. Sun, S. Okubo, Surface potential and gravity changes due to internal dislocations in spherical Earth. II: application to a finite fault, Geophys. J. Int. 132 (1998) 79–88.

[17] X.Q. Ma, N. Kusznir, Effects of rigidity layering, gravity and stress relaxation on 3-D subsurface fault displacement fields, Geophys. J. Int. 118 (1994) 201–220.

[18] F.F. Politz, Postseismic relaxation theory on the spherical Earth, Bull. Seismol. Soc. Am. 82 (1992) 422–453.

[19] F.F. Politz, Gravitational viscoelastic postseismic relaxation in a layered spherical Earth, J. Geophys. Res. 102 (1997) 17921–17941.

[20] A. Piersanti, G. Spada, R. Sabadini, M. Bonafede, Global postseismic deformation, J. Geophys. Res. 120 (1995) 544–566.

[21] R. Sabadini, A. Piersanti, G. Spada, Toroidal/poloidal partitioning of global post-seismic deformation, Geophys. Res. Lett. 21 (1995) 985–988.

[22] M. Vallée, M. Bouchon, Imaging coseismic rupture in far field by slip patches, Geophys. J. Int. 156 (2004) 615–630.

[23] D.H. Christensen, S.L. Beck, The rupture process and tectonic implications of the great 1964 Prince William Sound earthquake, Pure Appl. Geophys. 142 (1994) 29–53.

[24] C. Zweck, J.T. Freymueller, S.C. Cochen, Three-dimension elastic dislocation modelling of the postseismic response to the 1964 Alaska earthquake, J. Geophys. Res. 107 (2002).

[25] J. Wahr, M. Molenaar, F. Bryan, The time variability of the Earths gravity field: hydrological and oceanic effects and their possible detection using GRACE, J. Geophys. Res. 103 (1998) 30,205–30,229.

[26] I. Velicogna, J. Wahr, H. Van den Dool, Can surface pressure be used to remove atmospheric contributions from GRACE data with sufficient accuracy to recover hydrological signals? J. Geophys. Res. 106 (2001) 16,415–16,434.

[27] G. Ramillien, A. Cazenave, O. Brunau, Global time variations of hydrological signals from GRACE satellite gravimetry, Geophys. J. Int. 158 (2004) 813–826.

[28] E.L. Lehmann, Testing of Statistical Hypotheses, John Wiley, New York, NY, 1986, 602 pp.

[29] D.F. Barnes, Gravity changes during the 26 years following the 1964 Alaskan earthquake, Geological Studies in Alaska, USGS Professional Paper, vol. 1614, 1997, pp. 115–122.

[30] J.C. Savage, J.L. Svarc, W.H. Prescott, W.K. Gross, Deformation across the rupture zone of the 1964 Alaska earthquake, 1993–1997, J. Geophys. Res. 103 (1998) 21275–21283.

[31] J.T. Freymueller, S.C. Cohen, H.J. Fletcher, Spatial variations in present-day deformations, Kenai Peninsula, Alaska, and their implications, J. Geophys. Res. 105 (2000) 8079–8101.